# Intermittent induced seismicity during the multi-year operation of a geothermal reservoir

Olivier Lengliné, Vincent Maurer, Anthony Yorillo

Geophysical Journal International

*Geophys. J. Int.* (2025) **242,** 1–12
Advance Access publication 2025 May 5
Research Paper

https://doi.org/10.1093/gji/ggaf160

# Intermittent induced seismicity during the multiyear operation of a geothermal reservoir

O. Lengliné [1], V. Maurer[2] and A. Yorillo[1,2]

[1] *EOST/ITES, Université de Strasbourg/CNRS,* UMR7063, 5 rue René Descartes, 67084 Strasbourg Cedex, *France. E-mail: lengline@unistra.fr*
[2] *ES-Geothermie,* 26 boulevard du président Wilson, 67000 Strasbourg, *France*

Accepted 2025 April 29. Received 2025 April 28; in original form 2024 October 11

## SUMMARY

Understanding the mechanical behaviour of a fractured geothermal reservoir during its operation phase, when a sustained circulation of fluid is taking place, is of crucial importance for the appraisal of this technology. This knowledge is also essential for understanding natural fault systems that exhibit fluid-induced seismicity, as the geothermal reservoir serves as a small-scale analogue to these systems. Here, we analyse the seismicity of a geothermal reservoir in France, which has been the primary target for heat exploitation over the last 8 yr. Fluid circulation in the granite has been maintained along a main fractured zone through pathways with enhanced permeability thanks to the continuous injection of fluid from a single well. We show that the seismicity occurring during the operation of this reservoir exhibits a progressive expansion outpacing the zone initially activated during the hydraulic stimulation. We also show that most recorded earthquakes are clustered in time within discrete bursts that activate different portions of the fault system. The migration of the events included in these bursts indicates that they are likely related to aseismic transients developing over the creeping fault interfaces. It therefore demonstrates that the intermittency of the seismic activity characterizing earthquake swarms can arise naturally as the complex hydro-thermo-mechanical response of a system under continuous forcing conditions.

**Key words:** Fracture and flow; Europe; Induced Seismicity.

## 1 INTRODUCTION

During the development and the operation of deep geothermal plants in naturally fractured reservoirs, induced seismicity can occur at different stages (Zang *et al*. 2014). Usually, most of the seismicity is recorded at the initiation of the project, during the thermal and/or hydraulic stimulation of the reservoir (Cuenot *et al*. 2008; Deichmann & Giardini 2009; Albaric *et al*. 2014; Baisch *et al*. 2015). The purpose of such stimulations is generally to increase the hydraulic connectivity of the naturally fractured reservoir around the well (Baujard *et al*. 2017). In such stimulation phases, high volumes of fluid are injected at depth and lead generally to a large number of micro-earthquakes (Zang *et al*. 2014). While the analysis of the induced seismicity during such stimulation phases has been well documented in numerous studies (Deichmann & Giardini 2009; Diehl *et al*. 2017; Ellsworth *et al*. 2019; Lengliné *et al*. 2023; Zhou *et al*. 2024), there are however only few data available covering the operation period for enhanced geothermal systems (EGS). Some notable analyses covering operation periods are reported in (Majer *et al*. 2007; Azzola & Gaucher 2024; Koirala *et al*. 2024). As fluid is circulating within the geothermal loop, during the operation of the geothermal reservoir, seismic activity can still be noticed and needs to be appraised (Cuenot *et al*. 2010; Maurer *et al*. 2020a).

Although the induced activity during this stage is less documented, it is however crucial for a safe production of geothermal energy to maintain during the whole reservoir operation stage a low level of seismic activity. Understanding the occurrences and the development of the seismicity during the permanent circulation of fluid in the reservoir also allows us to track the evolution of a perturbed fault zone response over several years, subjected to a fluid circulation and the associated decrease of host rock temperature. It thus offers a unique opportunity to assess the response of a geological system with some knowledge on the forcing parameters affecting the seismicity under study. It also allows to operate an adequate and dedicated seismic monitoring network for capturing and documenting precisely the related seismic signal. As recent studies demonstrated that induced seismicity mostly result from stress changes caused by aseismic sliding ahead of the pressurized zone (Cornet *et al*. 1998; Guglielmi *et al*. 2015; Bhattacharya & Viesca 2019; Wynants-Morel *et al*. 2020), it therefore provides at the same time a window for analysing the activity of a creeping fault system driven by a constant influx of water. Here, we analyse the seismicity of the Rittershoffen geothermal reservoir in northern Alsace, France, in order to establish and understand the features of this induced seismicity during operation. This work has two main objectives. First, we want to identify the response of a deep naturally

fractured geothermal reservoir to a continuous injection of fluid over several years in order to appraise its evolution. Secondly, we aimed to draw links between the case studied here of the Rittershoffen geothermal reservoir and natural environments in which deep fluid circulations has been documented and which exhibit swarm like seismicity behaviour.

In terms of geological context, the deep geothermal field of Rittershoffen is located on the western margin of the NE–SW-striking central segment of the Upper Rhine Graben (URG). The URG extends on 300 km length, from Basel (Switzerland) in the south to Mainz (Germany) in the north. The lithospheric thinning in the URG is at the origin of a regional conductive heat flow density anomaly (Harlé *et al*. 2019), and the URG has been known for high-temperature gradient between 60 and 120 °C km$^{-1}$. From the surface to the top of the Middle Triassic (Muschelkalk), a conductive zone is observed, which is located above a multikilometric granitic convective zone into which geothermal fluids circulate (Pribnow & Schellschmidt 2000; Baillieux *et al*. 2013; Guillou-Frottier *et al*. 2013). The natural permeability in the convective zone is shown to be governed by the natural fracture system embedded in an approximately impermeable matrix (Dezayes *et al*. 2010; Genter *et al*. 2010; Sanjuan *et al*. 2016; Baujard *et al*. 2017). Consequently, natural faults play a major role in fluid circulation for geothermal reservoir in the URG and are the primary targets for operation. The shallow sedimentary layers of the URG are shifted by horsts and graben throughout globally N–S normal faults which accommodated the E–W former extension of the rift system. The main target of the Rittershoffen geothermal field is such a N–S permeable structure. The two wells of the Rittershoffen geothermal heat plant target the same fault zone, named Rittershoffen fault in the basement. This structure is well known from vintage 2-D seismic profiles, from two 2-D seismic lines acquired in 2013 (Baujard *et al*. 2017) and from a 3-D seismic survey of about 180 km$^2$ acquired in 2018 (Salaun *et al*. 2020). It is a globally N–S fault zone dipping roughly 70° to the West and showing an apparent vertical offset of more than 250 m. The fracture network was also observed from acoustic borehole wall imagery in the open-hole sections of GRT-1 and GRT-2 wells (Vidal et al. 2019). The main natural fractures oberved in GRT-1, are oriented with a global orientation of N15°E to N20°E with a dip of 80°W. In GRT-2, the main fracture set is oriented N155°E to N175°E with a dip of 80°E to 90°. The drilling of the injection well GRT-1 started in September 2012 and ended in December 2012. The well was drilled almost vertically and reached a depth of 2580 m MD (2562 m TVD). An important negative temperature anomaly was crossed by the GRT-1 well at around 2350 m TVD in the granite section (Baujard et al. 2017), certainly in relation to an open fracture associated to a branch of the local Rittershoffen normal fault (Vidal et al. 2016). After drilling, a reservoir development strategy was designed to enhance the connections between the well and the naturally fractured reservoir. A precise description of these operations is included in Baujard *et al*. (2017) and the associated induced seismicity is detailed in Maurer *et al*. (2020b) and more specifically in Lengliné *et al*. (2017a) for the hydraulic stimulation. These studies indicate that it still remains elusive whether the fault activated during these injections is indeed the one identified by the seismic survey, or whether it could also be an auxiliary fault present in the damaged zone of the main fault. The production well GRT-2 was drilled between March and July 2014. GRT-2 was drilled from the same well-pad than GRT-1 but is deviated to the North to reach 3196 m MD (2707m TVD). This second geothermal well was not stimulated because its hydraulic performance was good enough to be economical. The commissioning of the Rittershoffen geothermal plant started in May 2016 and exploits a geothermal brine to produce a thermal power of about 24 MWth (170°C, 250 m$^3$.h$^{-1}$). As of today, April 2024, 8519 local earthquakes have been recorded by the dedicated seismic network during the operation. Here, we analysed in details these events in order to document the activity during the stimulation and the operation of the geothermal reservoir. We notably show that the earthquake activity is not continuous but occurs during intense, migrating, seismicity bursts highlighting the complex brittle and ductile deformation of the fault system and the evolving channeling of the fluid pathway on the main structures over time.

## 2 DATA

### 2.1 Hydraulic data

During the most of the production period, the production flow-rate has been maintained at 270–310 m$^3$ h$^{-1}$, while the injection flow-rate is in the range 250–290 m$^3$ h$^{-1}$. The difference between the production and injection flow-rate results from the decrease of the fluid temperature between the two wells. The measured injection wellhead pressure has been steady in the range 5–7.5 bars for the period 2016–April 2018 and was artificially increased to 13–17 bars after April 2018 by the installation of a column with a reduced diameter down to 180 m in GRT-1 to keep the pressure above the bubble-point, avoiding scalings and degassing. This device therefore caused an apparent and immediate increase of the measure wellhead pressure but the downhole pressure was not impacted by this installation. Considering the head losses and a well-head pressure comprised between 13 and 15 bars at an injection flow-rate of 280 m$^3$ h$^{-1}$, the down-hole pressure could be estimated to be less than 5 bars. Apart from maintenance operations that require the plant to be shut down for periods of typically 2 weeks per year, the plant operates continuously and the hydraulic parameters remain stable (Fig. 1). Tracer tests also indicate that there exist an hydraulic connection between the two wells (Baujard *et al*. 2017). It is also documented from temperature logs, that the GRT-2 well intersects a main damage zone linked to the Rittershoffen fault at a depth of around 2400 m (Vidal *et al*. 2019) It is therefore established that a closed-loop circulation system is established between the two wells, the fluid circulating at depth along a main fractured zone through pathways with enhanced permeability (Baujard *et al*. 2017). The local normal fault intersected by the GRT-1 well is mainly a single pathway structure with a large hydrothermally altered and fractured damage zone. However, the same fault branch intersected by the GRT2 well is more complex and corresponds to a series of several permeable individual fractures.

### 2.2 Seismic network

The seismic network used to monitor the natural and the induced seismicity was described by Maurer *et al*. (2020b), mainly for the drilling and the stimulation operations (2012–2014). For the commissioning of the geothermal plant, 10 temporary stations were still operating to complete the permanent networks dedicated to the monitoring of the Soultz-sous-Forêts and the Rittershoffen geothermal plants. The temporary stations were removed in October 2017 and only the permanent networks remained after this date (Fig. 2). Most stations include three-component seismometers and are recording the ground motion continuously with a sampling frequency of 200 Hz.

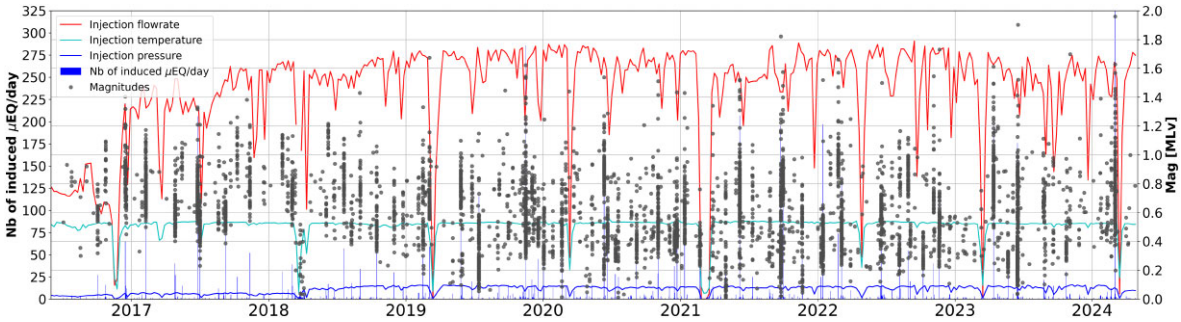


**Figure 1.** Variation of the injection flow-rate (red), injection temperature (light blue) and well-head pressure (dark blue) plotted with the daily seismicity rate of the Rittershoffen geothermal heat plant and the associated earthquake magnitudes (black circle). Absolute values of hydraulic parameters are not shown to respect confidentiality imposed by the operator of the plant. We can notice several shut-down periods of the heat plant indicated by sudden large drops of the injection hydraulic parameters.

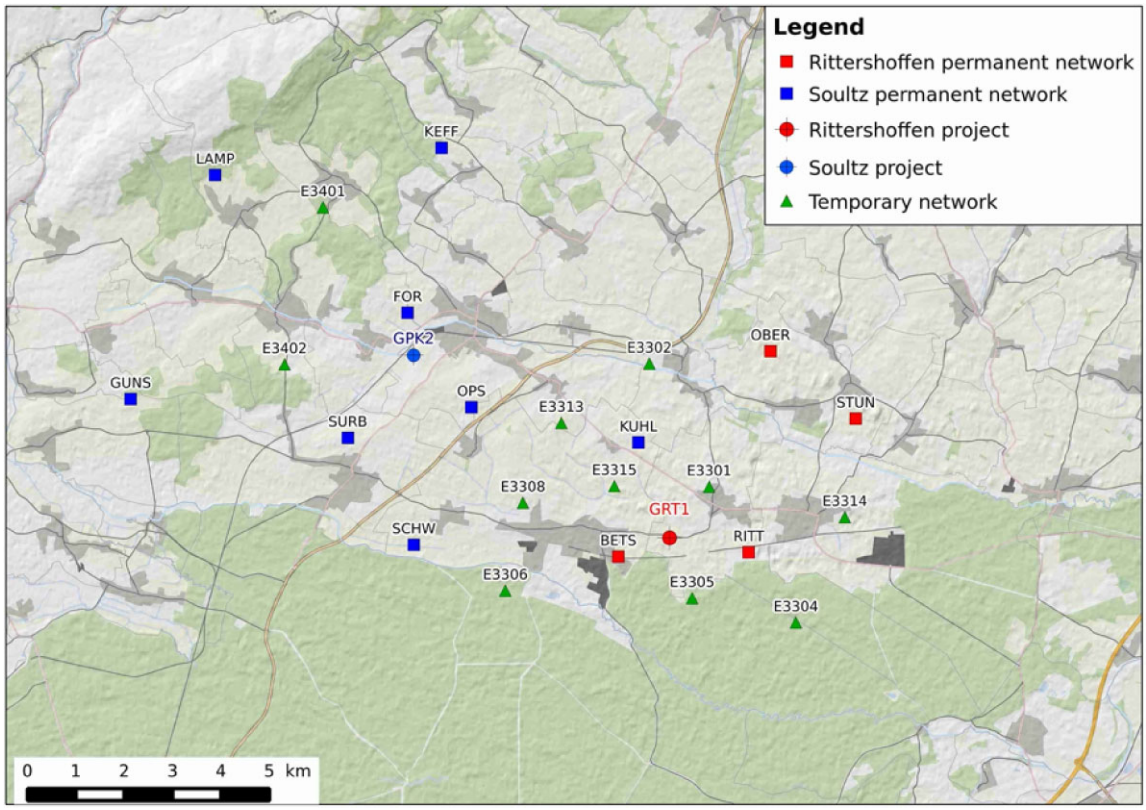


**Figure 2.** Map of the seismic network with the name of the stations used in this study. The temporary network stations were only in place up to October 2017. Some additional stations were also installed during the 2013 stimulation but are not displayed here and we refer to Maurer et al. (2020b) for a detailed description of the seismic network during this period.

### 2.3 Initial catalogue description

Since the commissioning of the plant in May 2016, a total of 6527 microseismic events have been detected and located in the direct vicinity of the project by the local seismic network. All these events have been carefully manually reviewed and picked and are routinely located using a 1-D velocity model of the area derived from a sonic-log in the GRT-1 well (Maurer *et al*. 2020b). Most of the events are located within a radius of 1 km around the open-hole section of the injection well GRT-1. As of today, April 2024, the maximum recorded local magnitude Mlv was 2.0 for an event that occurred on 2024 March 2. The maximum peak ground velocity associated to that event was 0.6 mm $s^{-1}$. For most of the events for which it has been possible to calculate a focal mechanism, strike-slip events were reported (Lengliné *et al*. 2017a; Maurer *et al*. 2020b). The initial seismicity catalogue thus comprises 8519 events including the 1992 events that took place before May 2016 (mostly during the stimulation phases of 2013). Among the thermal, chemical and hydraulic stimulation of GRT-1, the latter was the most seismogenic operation. The local magnitude of the seismicity ranged between −1.5 and 1.6 and the magnitude of completeness was estimated to be around 0. None of the induced events during the stimulations were felt by the population.

## 3 ABSOLUTE LOCATION

In a first step, we aim at improving the absolute location of the events of the catalogue before applying a subsequent relative relocation. In order to first improve this absolute location we take advantage of a newly derived 3-D velocity model of the area whose footprint extends over the two geothermal sites of Soultz-sous-Forêts and Rittershoffen. A litho-structural model has been compiled from a private contractor and was build upon a 3-D seismic acquisition acquired in 2018 around these sites. Specifically, the construction of the 3-D velocity model is based on the 1-D velocity profile of the initial model. Since the number of layers of the 1-D velocity model differ from the number of horizons picked in the 3-D seismic interpretation some layers of the 1-D velocity model were merged. Velocities were recalculated to keep the same vertical traveltime (harmonic mean speed). In addition, to take into account variations within these groupings, linear gradient layers with a velocity at the top and at the base of each layer were defined and extended to 3-D. To this end, the horizons of each homogeneous layer were located on surface seismic and exported so as to match these layers with those extracted from the 1-D model. Once the correspondence had been made, the velocities from the 1-D model corresponding to each of the layers were simply mapped into the 3-D model (Fig. S1, Supporting Information).

In order to correct for possible imprecision of this 3-D velocity model we decided also to take into consideration specific stations term corrections. In order to achieve this, we selected 10 earthquakes that took place during the early part of the stimulations in April and June 2013. These events have between 8 and 15 *P*-wave picks and between 6 and 12 *S*-wave picks. We assume that these events are located in the immediate vicinity of the intersection of the GRT1 well and the main conductive fault at a depth of 2352 m. Computing the theoretical traveltimes of these earthquakes in the 3-D velocity model and comparing with the one observed we can then derive theoretical station correction delays that we incorporate during the location process. The absolute location of all events in the catalogue is then performed using the presented 3-D velocity model and assuming the station correction extracted from the reference events. These new locations are closer to the injection well and correct an horizontal offset of around 500 m visible in the initial locations (Fig. S2, Supporting Information).

## 4 EARTHQUAKE RELOCATIONS

### 4.1 Methods

To give a more accurate picture of the seismicity, we then relocate all the events over the entire period. We first compute traveltime delays by correlating for each pair of events their *P*- and *S*-wave windows for each available pick. We set a *P*- and *S*-wave window duration of 0.8 and 1.0 s, respectively. The *P*-wave window is computed for vertical components seismograms while the *S*-window is applied to horizontal records. All signals are sampled at 200 Hz and filtered between 10 and 45 Hz when computing the correlations. We retained traveltime delays for a pair of events only if the correlation coefficient is higher than 0.5 for at least 8 *P* or *S*-window. Our final selection therefore includes 4.5 million *P*-wave traveltime differences and 7.0 million *S*-wave traveltime differences. These traveltime delays are then used in the Growclust3D algorithm that takes into account the traveltimes computed in the 3-D velocity model (Trugman & Shearer 2017). We relocate 6785 earthquakes out of the initial 8519 ones. We also estimated uncertainties from our relocations by performing 50 bootstrap iterations. The median horizontal and vertical uncertainties returned by this procedure are 26 and 32 m, respectively. Since the seismicity cloud as a whole may move relative to the initial location during relocation, we also apply a common shift to all resolved relocations. We therefore consider that the reference events used to calculate the station corrections are located at the reference position previously used. We deduce from these reference events an offset that we apply to all events of 72, 153 and −223 m in the east–west, north–south and depth directions, respectively (Fig. S3, Supporting Information).

### 4.2 Results

The relocation results demonstrate that the majority of the seismic activity is concentrated on a major single fault zone, the orientation of which is about N024°E close to the injection well and gradually approaches an NS direction as one moves further away from the injection point, specifically in the direction towards the production well (Fig. 3). It is also possible to evaluate the dipping of the activated structures by performing cross-sections at different points along the fault zone (Fig. S4, Supporting Information). The seismicity is generally aligned on a main structure that is dipping 77 degrees to the west, according to these cross-sections. Although the 3-D seismic results indicate that the overall direction and dip of the identified main structure agrees well with the location of the microseismicity, in detail this match is not perfect and it is difficult to match the two with certainty. This correlation is also hampered by the fact that, the reflection seismic method is largely ineffective within the granite, where the majority of the seismicity occurs, further limiting its applicability in this context. The identified structure was already visible from relocations of events that occurred during the stimulation phase of 2013, but it was unclear whether the events in the northern part, which occurred four days after the stimulation shut-in, were part of the same structure as the one activated during injection or not. The newly located events indicate that the earthquakes in the north are probably occurring on the same active fault system as the one observed at the injection point, although the fault's azimuth is slightly rotated, corresponding to a bend of the fault. We note however that some of the event positions appear to be dependent on the choice of the velocity model used during the relocation. Indeed, as visible in Fig. S5 (Supporting Information), although the main pattern emerging from event's relative location is preserved when the velocity model is changed, some branches can be slightly offset especially in the northern part. It is therefore difficult to be totally confident about whether the northern events are located on the same branch as the main fault or on a different branch. Regardless the exact positions of these few events, it is noteworthy that the direction of the main fault plane is likewise consistent with the inferred focal mechanisms of stimulation events (strike in the interval of 195 to 210°N) and is also in good agreement with the orientation of the main fracture zone mapped from borehole acoustic images in GRT-1 (Vidal *et al*. 2016; Maurer *et al*. 2020b). Some of the seismicity also appears to be on a slightly different structure, with a relatively lower dip angle (Fig. S4, Supporting Information). These results suggest that the vicinity of the well can certainly be described as a fault zone with secondary structures located around a main fault. Although most of the seismic activity occurs in the granitic basement, a small but significant portion takes place in the Triassic sandstones that lie directly above the granite. Overall, we observe that most of the

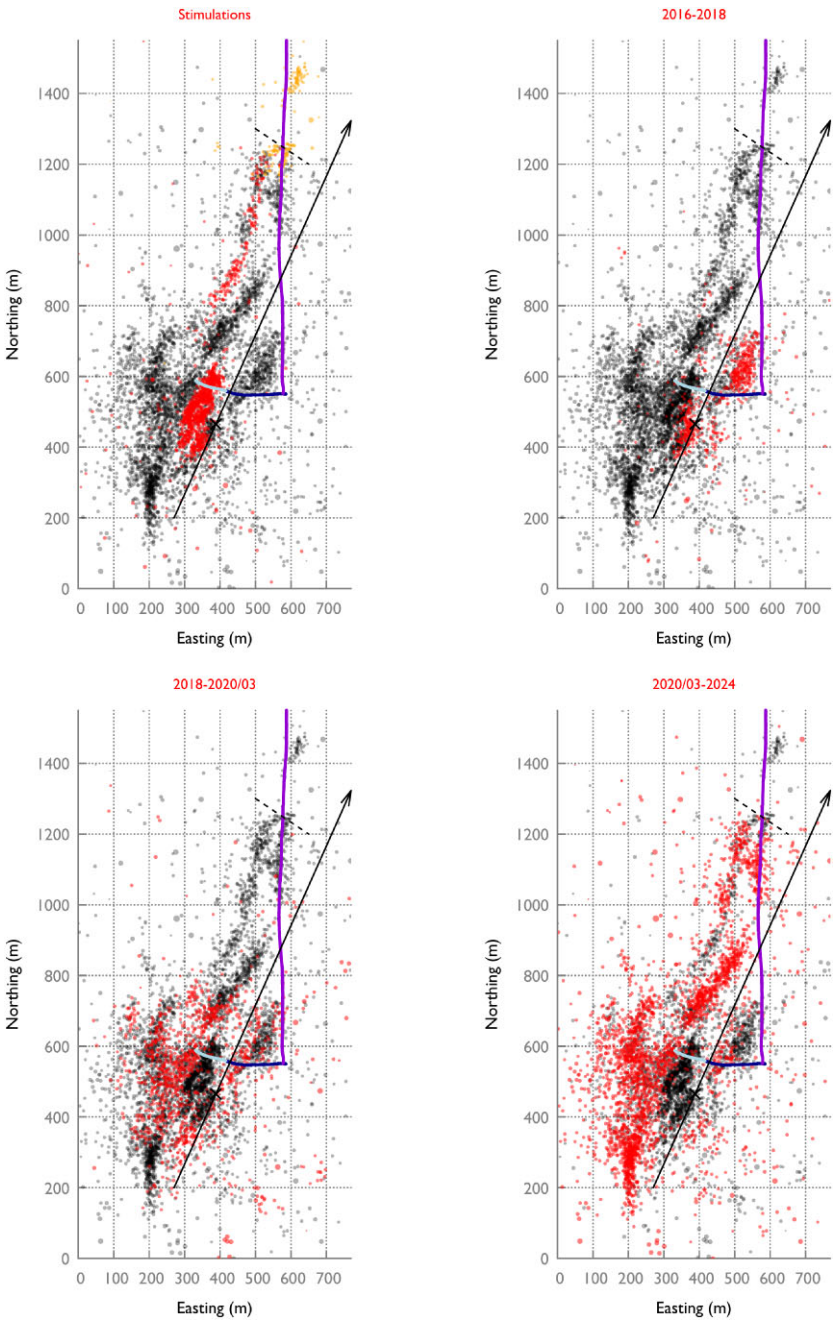


**Figure 3.** Map of all relocated events (black circles). The red circles correspond to events recorded during each of the indicated time period. The stimulations time period includes the injection phases in 2013 and the subsequent burst that took place 4 d after shut-in. For this stimulations period we also include, as yellow events, earthquakes that occurred during the drilling of the GRT-2 well. The two well trajectories, GRT-1 and GRT-2 are shown as a blue and a purple line, respectively. The open-hole section of the GRT-1 well is light blue while the cased section is in dark blue. The black arrow indicates the N24E oriented direction used to project events in Fig. 4. The black cross on this arrow gives the origin point along this line. The dashed black line indicates the maximum extent of seismicity to the north.

earthquakes tend to occur mainly on the major fault, namely the main fluid-carrying structure connecting the injection well to the production well.

When we examine the seismicity events across time, with a particular emphasis on the production period beginning in May 2016, we find two distinct patterns. First, we observe that the seismicity tends to migrate from the original injection point to the northern and southern terminations of the activated main structure over a period of several years. In fact, Figs 3 and 4 make this quite evident. Both show the position of seismicity at different times, which is clearly concentrated around the injection well during the early operating phase and gradually spreads throughout the entire defined structures. We also note that in the northern region, the seismic activity does not continue past the point at which it terminated, which was reached during the 2013 seismic burst that followed the stimulation phase. Conversely, we find that the seismicity propagates further southward than the seismic cloud visible at the time of the 2013 stimulation.

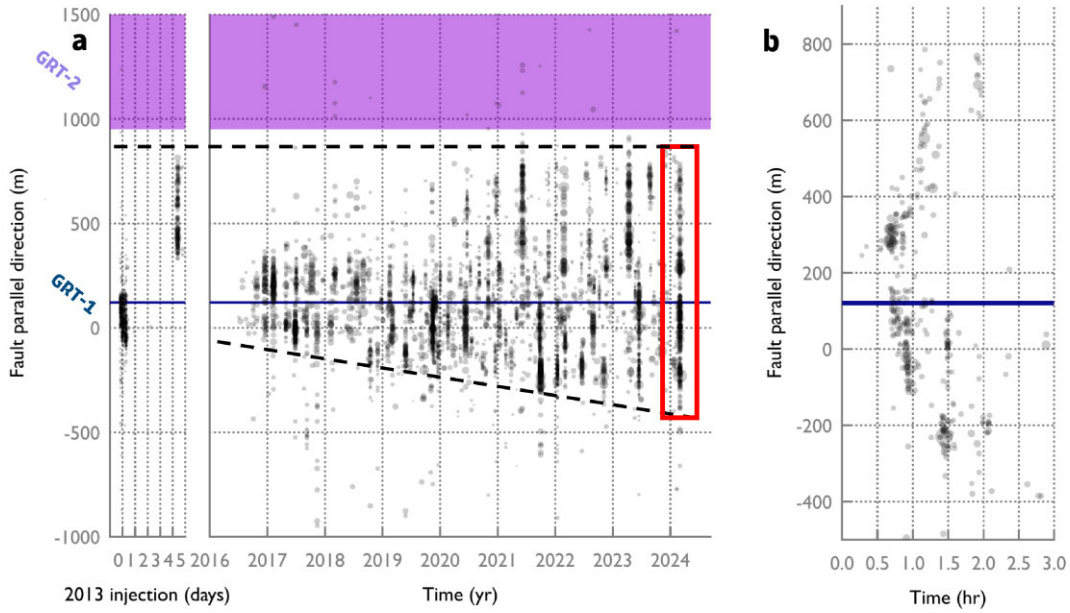


**Figure 4.** (a) Time space evolution of the seismicity. All relocated events are plotted as a function of time and their position along the main structure direction (N24E) shown in Fig. 3. The pale blue and purple colours refer to the location of the open hole section of the GRT-1 and GRT-2 well, respectively. The blue dashed lines delineate the global expansion of the seismicity. In the positive direction (north) the dashed line shows that the seismicity is not propagating further north to the activated area during the stimulation in 2013. In the south, we observe an overall global expansion of the seismic activity. The red rectangle isolate the March 2024 burst that is displayed in the zoom panel (b). (b) Zoom at the time of the March 2024 burst highlighting the migration of the events during the burst that takes place in both along strike directions and that extend over the whole imaged fault.

In addition, we observe that most seismicity is actually detected during discrete short intense episodes (Fig. S6, Supporting Information). These short episodes, taken together, illuminate the entire fault plane and are not restricted to a portion of the fault. The seismicity is generally dispersed over hundreds of meters during such burst of activity (Fig. 4a). Additionally, for some of these bursts, we can see a discernible migration of the earthquakes along the strike of the main structure. While some of these migration episodes are occurring in only one direction, they can be observed to occur in both directions simultaneously. These bursts of earthquakes comprise between few tens of events and up to several hundreds of events for the largest one so far that took place on 2024 March 2 (Fig. 4b).

We isolate these burst using the method proposed by Bakkum et al. (2014). A burst of earthquakes is defined when $N$ events happened in a time interval smaller than $T$. The time threshold $T$ and the number of events $N$ are calculated by looking at the probability distribution of the time intervals between earthquakes (see Fig. S7, Supporting Information). Indeed, the valley between the two peaks of this time intervals distribution was selected as the boundary between regimes and providing $T = 10$ hr and $N = 10$ events. It yields than $N$ consecutive earthquakes that happen in a time frame that is equal to or less than the threshold $T$ are attributed to a burst. The end of a burst is set when this condition is no longer met. The application of this algorithm to the events that occurred during the production phase of the reservoir leads to the identification of 81 bursts (Fig. S8, Supporting Information). To exclude possible outlier or badly located events that might be included in the bursts, we exclude, from the identified burst, events which are located at a distance that is larger than four times the median absolute deviation from the burst barycentre. From the initial population of 4204 burst events, this final procedure leaves us with 3977 events in 81 bursts comprising between 10 and 360 events.

The distributions of burst duration and burst recurrence time are displayed in Fig. S9 (Supporting Information) and highlight that burst are generally short (90 per cent of bursts have a duration of less than 10 hr). However, we note that during significant burst episodes, the heat plant operator typically temporarily reduces the flow-rate within 15 to 30 min of the onset of the seismic crisis. It is difficult to quantify the impact of this action on the seismic activity and on the burst duration but it may prevent the burst of getting any larger or lasting longer. The average duration of bursts with or without flow-rate reduction are nearly identical around 6 and 5 hr, respectively. But one should remember in interpreting these values that only the most intense bursts have been subject to a flow-rate reduction. The distribution displayed in Fig. S9 (Supporting Information) must be interpreted in the light of this information and does not therefore exactly correspond to the distribution of a system with constant loading conditions over the entire duration of the burst. The recurrence interval of these bursts does not exhibit any periodicity; instead, they appear to be clustered in time. The mean time interval between bursts is of 33 d while the median interval is 25 d.

During a burst, the stack evolution of the earthquake rate is computed by merging all the occurrence times of burst events relative to the time of the first event of each burst. We thus obtain a compound earthquake sequence representing the average behaviour of the seismicity rate during such burst sequences. We distinguish the 14 bursts for which a reduction in the flow-rate was imposed by the operator (generally the largest bursts) from the others 67 bursts for which no operation on the flow-rate was carried out in response to the seismicity. It is observed for both cases that, from the earliest time up to 30 min after the burst commencement, the seismicity rate, on average, decays with time from the burst onset as a power-law with an exponent 1/4 (Fig. 5). After then, there is a decrease in the seismicity rate occurring around 2000 s. This

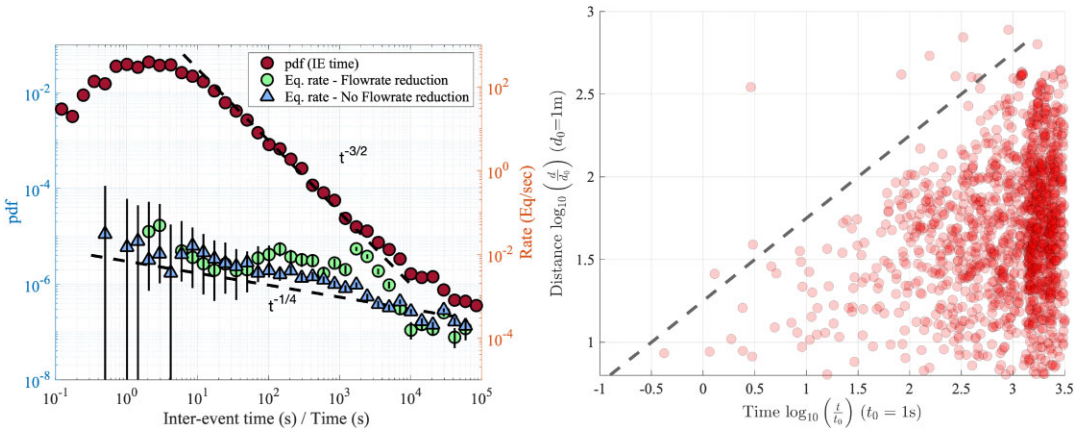


**Figure 5.** Left: Distribution of the time difference between two successive events in the catalogue considering only events occurring during the production phase (red circles). The distribution of the interevent time shows that events are well clustered in time and the distribution exhibit a power-law decay with an exponent of 1.5 for time intervals larger than 10 s. Blue triangles represent the averaged earthquake rate during burst sequences for which no flow-rate reduction was imposed (67 bursts episodes). It shows a low power-law decay rate with an exponent of 0.25. The green circles show the averaged earthquake rate during burst sequences for which a flow-rate reduction was imposed (14 sequences). For both earthquake rates, uncertainties are computed (vertical black line) assuming that the number of events in each time bin follows a Poisson's process. Right: Distance, from the first event of the burst, as a function of the time delay, from the first event of the burst, for all identified events belonging to a burst sequence (red dots). The dashed line indicates the $d \propto \sqrt{(t)}$ relation and evidences that the seismicity front during burst sequence is migrating according to such a relation.

drop of the seismicity rate is more pronounced for bursts associated with a flow-rate reduction, suggesting that this action may have an effect on burst termination. We however remain cautious about this conclusion given the limited number of analysed burst sequences. We also note that the evolution of the seismicity rate during a burst is in sharp contrast with the probability density function (pdf) that describes the recurrence time between two successive earthquakes in the catalogue (Fig. 5). This distribution indicates a much more pronounced time clustering of the earthquakes activity indicating that burst episodes are actually formed as a succession of cascading events.

To investigate the space-time behaviour of the seismicity during these bursts we represent as a function of the time from the first event of each burst, the epicentral distance from this first event. We already observed for some particular individual bursts a clear migration of the events that takes place in the strike direction both in the flow direction and in the opposite direction. Here, our intent is to highlight if there is any general characteristic of the migration from these bursts. Fig. 5 demonstrates that there exists a time space coupling of the dynamic behaviour of the propagation of these bursts and that the seismicity illuminated during these bursts is expanding up to a distance, $d$ as a function of the time, $t$ compatible with a diffusive regime characterized by $d \propto \sqrt{t}$. Unfortunately, a clear direction of propagation can only be observed for the few largest swarms which prevents us for determining if there exists a preferred direction of migration during these bursts.

Finally, in order to determine whether short timescale variations in fluid pressure may have influenced the emergence of these bursts we also compared the seismicity rate during burst sequence and the recorded wellhead pressure (Fig. 6). While the long-term evolution of the wellhead pressure remains nearly constant over several years (Fig. 1), short-term fluctuations in fluid pressure are significant from one burst to another (Fig. 6). It is however clear from looking at the evolution of the median wellhead fluid pressure over all sequences (with or without flowrate reduction) that the median pressure does not seem to vary significantly in the hours preceding a seismic burst. The fluctuations of the hydraulic parameters before the occurrence of a burst do not seem to show any characteristic trend indicating an impeding seismic activity. This clearly indicates that the occurrence of seismic burst is not linked to a direct change of the hydraulic loading condition imposed to the reservoir.

## 5 DISCUSSION

The seismicity occurring during the 2016–2024 period and associated with the operation of the Rittershoffen geothermal reservoir highlights several important features.

### 5.1 Long-term seismicity change

First we note that the seismic activity is expanding from the injection point. This activity progressively spreads over several years, and partially re-occupy some portions of the fault zone initially activated at the time of the stimulation. We note that on the northern part, it is remarkable that the seismicity halts near the net zero pressure boundary. This boundary corresponds to the point where the overpressure from the injection well balances the underpressure from the production well, resulting in a net pressure of zero. This balance likely establishes a limit for fluid overpressure to progress further northward, thereby preventing additional seismicity in that area. Another explanation of this limit in the expansion could be the existence of a geological structure, not visible in the 3-D-seismic, that acts as a physical barrier.

Building on the previous observations, several scenarios can be proposed to explain the general trend of migrating seismicity and its expansion over the course of several years. A first hypothesis would be to consider that due to mineral precipitation since the stimulation of the reservoir the fault progressively cemented and strengthened between the time of the stimulation in 2013 and the beginning of the operation phase in 2016. Even if the injectivity index of the well GRT-1 remained stable between the time of the stimulation and the commissioning of the plant, the injection flow-rate progressively increased between 2016 and the end of 2017 from 170 to 270 $m^3\ hr^{-1}$, (Fig. 1) and it never exceeded the 285 $m^3\ hr^{-1}$ reached during the stimulation. As a consequence, the perturbation

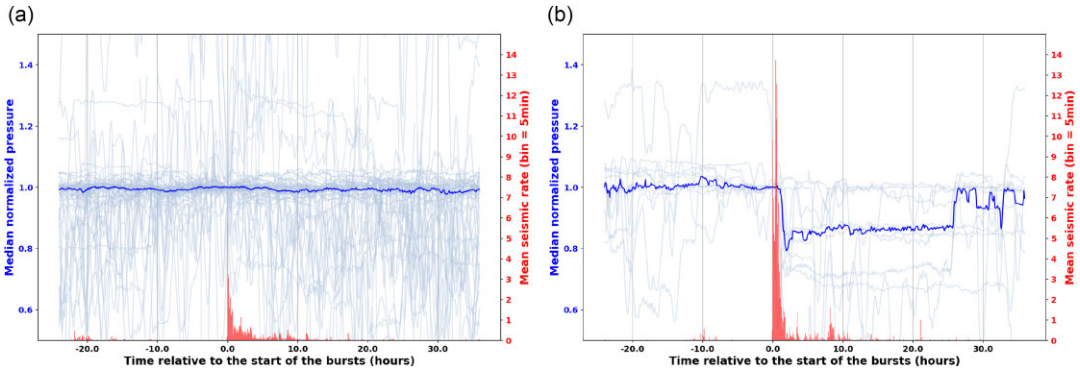


**Figure 6.** Evolution of the average seismicity rate (in red) as a function of time since the burst onset. The wellhead pressure for each identified burst is depicted as light blue curve. For each curve, the pressure is normalized to the value recorded at the start of the burst. The dark blue curve is a median of the fluid pressure variation computed over all sequences. Panel (a) is representative of the 67 sequences without flow-rate reduction while panel (b) corresponds to sequences for which a flow-rate reduction was imposed. We can note for these sequences a small increase in seismic activity recorded at around 9 hr after the burst onset in conjunction with a rise in flowrate (returning to the pre-burst level) and in the measured pressure (as can be seen on the individual pressure curves).

caused by the injection of water on the fault at the commissioning of the heat plant which is of much more limited amplitude than the stimulation one, first reactivates only an area close to the injection well. However as the hydraulic parameters remains steady since the end of 2017, it implies that the growth of the seismic cloud after this date cannot result from an increasing amplitude of the fluid perturbation. A second scenario would be to consider the role of the thermal stress caused by the continuous circulation of the cold (75-80 °C) re-injected fluid which has been proposed to cause potential perturbation within geothermal reservoirs modifying the local stress conditions and promoting earthquake nucleation (Martínez-Garzón et al. 2014; Im & Avouac 2021). In this hypothesis, the thermal contraction of the rock near the circulating fluid activates critically loaded faults at some distance through thermo-elastic effect. In that case, the locations of the seismic events are therefore not directly correlated with the presence of the fluid. As we might expect that the temperature perturbation within the reservoir is progressively expanding and its amplitude increasing, this could also provide an alternative mechanism for the increasing reach of the seismic cloud. A last explanation could also be related to a progressive weakening of the fault zone interface similar to a stress corrosion mechanism due to the prolonged exposition of the rocks on the fault interface to a the geothermal fluid. In such a scenario, an improved connection between the injection point and the reservoir's faults is progressively established, first close to the well, then further and further away, asymmetrically towards the production well. Such weakening is therefore facilitating the condition for earthquake or slow slip occurrence (Wintsch et al. 1995; Yehya & Rice 2020).

### 5.2 Channelling effect

Our relocation results also show some channelling effects of the fluid circulation within the fault zone subjected to a continuous fluid injection. Indeed we observed that the seismicity developed in different locations of the same fault zone over time. For example as visible in Fig. 3 we can observe that in the northern part of the fault (further north than the injection location) two parallel streaks of seismicity are visible. Here, we highlight that these two different streaks of the northern fault zone are not activated at the same time. For example, the westernmost streak was active during the burst which occurred just 4 d after the cessation of the stimulation in 2013. The other streak on the contrary was active years later during the operation period while the first one remains silence since. Hypothesizing that the seismicity is a good marker of the pressurized fluid pathway (Shapiro & Dinske 2009) it implies that the pressurized fluid circulate along channelized paths that vary over time. This variation of the fluid pressure pathway over different possible channels could results from multiple factors. It can notably results from the perturbation of the fault plane environment due to the long-term fluid-rock interaction through mineral precipitation or dissolution, progressive cooling of the host rock, vein dilatation, or creation of new fractures (Yasuhara & Elsworth 2006; Frery *et al*. 2015; Dobson *et al*. 2021). It is also possible that these different channels are activated at various levels of fluid pressure such that the activated branch just after the 2013 injection corresponds to a fluid pressure level not seen since then. This exemplifies the fact that the fluid circulation on faults within a geothermal reservoir should be modelled by a more complex geometry than simply two parallel planes and that such medium may undergo evolution over time (Neuville et al. 2010). The evolving topography of the interface and the change of the host rock physical properties can therefore lead to modification of the channelling effect over time and change the seismicity location.

We also note that although tracer tests demonstrated a direct connection between the injection and production wells, they also revealed that most of the water originates from the reservoir, with only a small fraction being recirculated. Continuous chemical monitoring of the geothermal water has shown no significant changes in water composition during the production phase while the flowing water opened new pathways and activated fracture systems that were previously untouched. This suggests a homogeneous composition across the geothermal reservoir. Together, these observations confirm the open nature of the reservoir and the large-scale homogeneity of the geothermal fluids within it.

### 5.3 Intermittent behaviour

A major characteristic of the seismicity taking place during the production phase at the Rittershoffen geothermal reservoir is its intermittency. It is possible to draw some comparisons with other geological systems that exhibit a comparable behaviour. We indeed observed that in fluid-induced seismicity, there have been reported instances of these sporadic bursts of activity, particularly in relation to long-term fluid injection (Park *et al*. 2020;

Schultz *et al*. 2023). This tendency is more infrequently seen during short-term injection episodes, when the activity seems to be considerably less time-clustered and more continuous (Langenbruch *et al*. 2011; Fischer & Hainzl 2021). For example, during the hydraulic simulations that occurred in the nearby Soultz-sous-Forêts reservoir or in the Rittershoffen reservoir, the seismicity rate appears quite steady and modulated mostly by the variations of the injection pressure (Cauchie *et al*. 2020; Maurer *et al*. 2020b). This difference in seismicity behaviour between circulation and stimulation can maybe be explained by the fact that during the stimulation, the seismicity rate is so high that these bursts are actually present but follow one another at a high rate, creating a high and constant apparent seismicity rate. In many natural environments, particularly those where it is assumed that fluid activity is the main driver, the organization of seismicity is similarly well defined by a steady long-term expansion interspersed with multiple short episodes exhibiting a rapid migration, as observed here (De Barros *et al*. 2020; Fischer *et al*. 2023). It has also been established that environments that host slow slip events, such as on the deep segment of the San-Andreas fault at Parkfield or on the Mexican subduction interface, also exhibit the same tendency (Ghosh *et al*. 2010; Houston *et al*. 2011; Wu *et al*. 2015; Gombert & Hawthorne 2023). All these systems have the property to exhibit a similar intermittent activity characterized by swarm of events without any clear mainshock and show sign of activity migration of the activity. For example, the statistical analysis of the recurrence time of earthquake and their decay rate during bursts as reported in Fig. 5 are very similar to the results conducted on Low Frequency Earthquakes on three different tectonic settings (Lengliné et al. 2017b).

This discrete feature of the activity that takes place during short, localized avalanche of events is well described as a characteristic of creeping faults (Jolivet & Frank 2020). Indeed, in places where appropriate instrumentation is available, slow slip transients have been observed to occur concomitantly with seismicity bursts. Numerical models, including asperities on a creeping fault infiltrated by fluids, reproduce the observed burst like seismicity pattern and link this observation to the occurrences of slow slip migration on the fault interface (Dublanchet & De Barros 2021).

It therefore suggests that the observed intermittent activity is caused by the repeated aseismic motion propagating on various portions of the activated fault zone (Jolivet *et al*. 2015). The aseismic slip is promoted by the fluid injection reducing the effective normal stress on the fault plane in an otherwise already favourable environment for aseismic motion in a frictional sense due to the shallow depth (reduced normal stress) and hot environment (at least for the geothermal reservoir) (Guglielmi *et al*. 2015; Wynants-Morel *et al*. 2020). We note as well that massive secondary clay minerals like illite wear are commonly observed in the fault damage zones of the Rittershoffen geothermal site (Genter *et al*. 2010; Vidal *et al*. 2019) and could contribute to aseismic fault movement (Meller *et al*. 2014). It is important to point out that the hydraulic properties (injection flow-rate and pressure) of the Rittershoffen geothermal reservoir is almost constant during the whole operation phase. Hence, the discrete response of the stimulated fault zone is not a response to a variable loading. It rather points out that the system (the fault zone subjected to the injection) while loaded by a continuous source, organizes itself to respond in such an intermittent way. Establishing the link between these bursts and the evolving condition within the reservoir at the Rittershoffen geothermal reservoir therefore provides opportunity to address the mechanics of creeping faults and earthquake swarms, especially those in which the role of fluid is assumed to be important.

## 6 CONCLUSION

The sustained fluid injection in the Rittershoffen geothermal reservoir enhanced pre-existing pathways within the granite that allow for the circulation of geothermal fluid, facilitating heat extraction. Over time, the seismicity within the reservoir did not remain confined to the zone initially activated during the hydraulic stimulation but instead progressively expanded beyond it. This expansion suggests that the fluid is influencing a growing portion of the fault network, potentially altering the stress state over a larger area.

The analysis of the seismicity patterns at Rittershoffen further reveals that most of the recorded earthquakes are not evenly distributed over time but instead occur in discrete, short clustered sequences. These bursts of seismic activity often activated different parts of the fault system, demonstrating the complex interplay between fluid injection, fault dynamics and seismicity. The migration of these seismic events within the different sequences suggests that they are likely linked to aseismic transients occurring along the fault interface. These transients represent slow, creeping movements within the fault, which can drive seismic activity at specific times.

This observation provides valuable evidence that the intermittent nature of seismic activity, often characteristic of earthquake swarms, can arise in geothermal reservoirs. It highlights the complex hydro-thermo-mechanical response of the reservoir under continuous fluid injection, where seismicity is not a simple, stationary process but rather emerges from the intricate dynamics of the fault system. Understanding these processes is crucial for managing geothermal operations.

## ACKNOWLEDGMENTS

First of all, the authors thank both ECOGI and the EEIG "Heat Mining" for sharing geoscientific and technical data from Rittershoffen and Soultz-sous-Forêts geothermal plants, respectively. We thank the people of ESG, Clement Baujard, Albert Genter and Carole Glaas for their numerous comments regarding the hydraulic and geological description of the Rittershoffen reservoir. We acknowledge Christophe Barnes from GIM-labs for providing us the 3-D velocity model. This paper has benefitted from helpful reviews by R. Schultz and T. Fischer, which helped us to improve the quality of our work. Michael J. Heap helped us with grammatical assistance. This work was carried out in the framework of the Interdisciplinary Thematic Institute GeoT as part of the ITI 2021–2028 programme of the University of Strasbourg, CNRS and Inserm. It was supported by ANR PrESENCE (ANR-21-CE05-0033-01), IdEx Unistra (ANR-10-IDEX-0002), SFRI-STRAT'US project (ANR-20-SFRI-0012) under the framework of the French Investments for the Future Program. This work was also carried out within the framework of the AIS project (ANR ANR-22-FAI2-0008-02) and the INSeis project under contract ANR-22-CE49-0018.

## SUPPORTING INFORMATION

Supplementary data are available at *GJIRAS* online.

**Figure S1.** Cross-section of the 3-D velocity model used for location and relocation of the seismic events. The different colours correspond to various *P*-wave velocities that were derived from the sonic log in GRT-1. The depth variations of the interfaces are obtained from seismic profiles across the area. The black and grey

lines correspond to the trajectories of GRT-1 and GRT-2 wells, respectively.

**Figure S2**. Absolute location of all events in the initial cataloge using the 1-D velocity model as presented in (Maurer *et al*. 2020b) (red circles) or using the 3-D velocity model including station correction terms (black circles). The blue and purple lines indicate the GRT-1 and GRT-2 well, respectively. We observe that the seismic cloud is more clustered around the injection well using the 3-D velocity model.

**Figure S3**. Map showing the all the relocated events (black circles). The reference events that have been used to shift all event positions are indicated in red. We can observe that most of them are well clustered. The barycentre of this cluster is matched with the position of the identified fault plane intersecting the GRT-1 well.

**Figure S4.** Top: map showing the events that are displayed on the two cross-section profiles A–A′ and B–B′. Bottom: Distance along profile as a function of depth for the events along the two profiles. The blue line is the projected trajectory of the GRT-1 well. The grey polygon represent the projection of the Rittershoffen fault, as observed from seismic. The stratigraphic log obtained along GRT-1 also shown on the right.

**Figure S5.** Relocation results obtained when the relocation is performed using different velocity models. The left figure shows the results using the 3-D model of this study. The central figure shows the relocation using a coarser and 3-D velocity model derived from the GEORG database and presented in Lengliné *et al*. (2023). The figure on the right shows the result of the relocation using the 1-D velocity model. Each dot represents a relocated event and the colour of the dot refers to its depth.

**Figure S6.** Time difference between two successive events in the relocated catalogue as a function of time. Burst sequences appear as vertical streaks of points.

**Figure S7**. Probability of the recurrence interval between seismic events in the catalog as a function of inter-event interval. The inter-event interval depends on the parameter $N$ that is set as the threshold number of events for defining a burst. We observed that the computed distributions (varying the quantity $N$ in the tested interval) exhibits a minimum around 10 hours for $N$ close to 10. We therefore fix the thresholds $T$ and $N$ based on this observation.

**Figure S8**. Time space evolution of the seismicity. All relocated events are plotted as a function of time and their position perpendicular to the cross-section direction, N114E. Dark circles indicate events that do not belong to a burst while colour circles indicate identified burst events. Each burst is represented by a different colour.

**Figure S9**. Left: distribution of burst recurrence times for the identified 81 bursts. Right: distribution of the burst durations. For burst durations we distinguish bursts for which a flow-rate reduction controlled by the operator was imposed (14 sequences in orange) and bursts with no associated flow-rate reduction (blue).

Please note: Oxford University Press is not responsible for the content or functionality of any supporting materials supplied by the authors. Any queries (other than missing material) should be directed to the corresponding author for the paper.

## DATA AVAILABILITY

All waveforms used in this study belong to ES-G company. The hydraulic data shown in Fig. 1 are the exclusive property of ECOGI. Some of the data processing is accomplished using Obspy (Beyreuther *et al*. 2010) and Matlab software (MathWorks 2020). Most figures have been made with Gnuplot (Williams *et al*. 2010) and some with the GMT (Wessel *et al*. 2019) software.

## REFERENCES


Albaric, J., Oye, V., Langet, N., Hasting, M., Lecomte, I., Iranpour, K., Messeiller, M. & Reid, P., 2014. Monitoring of induced seismicity during the first geothermal reservoir stimulation at Paralana, Australia, *Geothermics,* **52,** 120–131.

Azzola, J. & Gaucher, E., 2024. Seismic monitoring of a deep geothermal field in Munich (Germany) using borehole distributed acoustic sensing, *Sensors,* **24**(10), 3061. doi:10.3390/s24103061.

Baillieux, P., Schill, E., Edel, J.-B. & Mauri, G., 2013. Localization of temperature anomalies in the upper rhine graben: insights from geophysics and neotectonic activity, *Int. Geol. Rev.,* **55**(14), 1744–1762.

Baisch, S., Rothert, E., Stang, H., Vörös, R., Koch, C. & McMahon, A., 2015. Continued geothermal reservoir stimulation experiments in the Cooper basin (Australia), *Bull. seism. Soc. Am.,* **105**(1), 198–209.

Bakkum, D.J., Radivojevic, M., Frey, U., Franke, F., Hierlemann, A. & Takahashi, H., 2014. Parameters for burst detection, *Front. Comput. Neurosci.,* **7,** 193. doi:10.3389/fncom.2013.00193.

Baujard, C., Genter, A., Dalmais, E., Maurer, V., Hehn, R., Rosillette, R., Vidal, J. & Schmittbuhl, J., 2017. Hydrothermal characterization of wells GRT-1 and GRT-2 in Rittershoffen, France: implications on the understanding of natural flow systems in the Rhine Graben, *Geothermics,* **65,** 255–268.

Beyreuther, M., Barsch, R., Krischer, L., Megies, T., Behr, Y. & Wassermann, J., 2010. Obspy: A python toolbox for seismology, *Seismol. Res. Lett.,* **81**(3), 530–533.

Bhattacharya, P. & Viesca, R.C., 2019. Fluid-induced aseismic fault slip outpaces pore-fluid migration, *Science,* **364**(6439), 464–468.

Cauchie, L., Lengliné, O. & Schmittbuhl, J., 2020. Seismic asperity size evolution during fluid injection: case study of the 1993 Soultz-sous-Forêts injection, *Geophys. J. Int.,* **221**(2), 968–980.

Cornet, F., Helm, J., Poitrenaud, H. & Etchecopar, A., 1998. Seismic and aseismic slips induced by large-scale fluid injections, in *Seismicity Associated with Mines, Reservoirs and Fluid Injections,* pp. 563–583, Springer.

Cuenot, N., Dorbath, C. & Dorbath, L., 2008. Analysis of the microseismicity induced by fluid injections at the egs site of Soultz-sous-Forêts (Alsace, France): implications for the characterization of the geothermal reservoir properties, *Pure appl. Geophys.,* **165,** 797–828.

Cuenot, N., Dorbath, L., Frogneux, M. & Langet, N., 2010. Microseismic activity induced under circulation conditions at the egs project of Soultz-sous-Forêts (France), in *Proceedings of the World Geothermal Congress, Bali, Indonesia,* pp. 25–29.

De Barros, L., Cappa, F., Deschamps, A. & Dublanchet, P., 2020. Imbricated aseismic slip and fluid diffusion drive a seismic swarm in the Corinth Gulf, Greece, *Geophys. Res. Lett.,* **47**(9), e2020GL087142. doi:10.1029/2020GL087142.

Deichmann, N. & Giardini, D., 2009. Earthquakes induced by the stimulation of an enhanced geothermal system below basel (Switzerland), *Seismol. Res. Lett.,* **80**(5), 784–798.

Dezayes, C., Genter, A. & Valley, B., 2010. Structure of the low permeable naturally fractured geothermal reservoir at Soultz, *Comptes Rendus Geoscience,* **342**(7–8), 517–530.

Diehl, T., Kraft, T., Kissling, E. & Wiemer, S., 2017. The induced earthquake sequence related to the st. gallen deep geothermal project (Switzerland): fault reactivation and fluid interactions imaged by microseismicity, *J. Geophys. Res. Solid Earth,* **122**(9), 7272–7290.

Dobson, P.F., Kneafsey, T.J., Nakagawa, S., Sonnenthal, E.L., Voltolini, M., Smith, J.T. & Borglin, S.E., 2021. Fracture sustainability in enhanced geothermal systems: experimental and modelling constraints, *J. Energy Resour. Technol.,* **143**(10), 100 901. doi:10.1115/1.4049181.

Dublanchet, P. & De Barros, L., 2021. Dual seismic migration velocities in seismic swarms, *Geophys. Res. Lett.,* **48**(1), e2020GL090025. doi:10.1029/2020GL090025.

Ellsworth, W.L., Giardini, D., Townend, J., Ge, S. & Shimamoto, T., 2019. Triggering of the Pohang, Korea, earthquake (*M* w 5.5) by enhanced geothermal system stimulation, *Seismol. Res. Lett.,* **90**(5), 1844–1858.

Fischer, T. & Hainzl, S., 2021. The growth of earthquake clusters, *Front. Earth Sci.,* **9,** 638 336. doi:10.3389/feart.2021.638336.

Fischer, T., Hainzl, S. & Vlček, J., 2023. Fast migration episodes within earthquake swarms, *Geophys. J. Int.,* **235**(1), 312–325.

Frery, E. *et al.*, 2015. Evolution of fault permeability during episodic fluid circulation: evidence for the effects of fluid–rock interactions from travertine studies (Utah–USA), *Tectonophysics,* **651,** 121–137.

Genter, A., Evans, K., Cuenot, N., Fritsch, D. & Sanjuan, B., 2010. Contribution of the exploration of deep crystalline fractured reservoir of soultz to the knowledge of enhanced geothermal systems (egs), *Comptes Rendus Geoscience,* **342**(7–8), 502–516.

Ghosh, A., Vidale, J.E., Sweet, J.R., Creager, K.C., Wech, A.G., Houston, H. & Brodsky, E.E., 2010. Rapid, continuous streaking of tremor in cascadia, *Geochem. Geophys. Geosyst.,* **11**(12), doi:10.1029/2010GC003305.

Gombert, B. & Hawthorne, J.C., 2023. Rapid tremor migration during few minute-long slow earthquakes in cascadia, *J. Geophys. Res. Solid Earth,* **128**(2), e2022JB025034. doi:10.1029/2022JB025034.

Guglielmi, Y., Cappa, F., Avouac, J.-P., Henry, P. & Elsworth, D., 2015. Seismicity triggered by fluid injection–induced aseismic slip, *Science,* **348**(6240), 1224–1226.

Guillou-Frottier, L., Carrė, C., Bourgine, B., Bouchot, V. & Genter, A., 2013. Structure of hydrothermal convection in the upper Rhine Graben as inferred from corrected temperature data and basin-scale numerical models, *J. Volc. Geotherm. Res.,* **256,** 29–49.

Harlé, P. *et al.*, 2019. Heat flow density estimates in the upper rhine graben using laboratory measurements of thermal conductivity on sedimentary rocks, *Geotherm. Energy,* **7,** 1–36.

Houston, H., Delbridge, B.G., Wech, A.G. & Creager, K.C., 2011. Rapid tremor reversals in Cascadia generated by a weakened plate interface, *Nat. Geosci.,* **4**(6), 404–409.

Im, K. & Avouac, J.-P., 2021. On the role of thermal stress and fluid pressure in triggering seismic and aseismic faulting at the Brawley geothermal field, California., *Geothermics,* **97,** 102 238. doi:10.1016/j.geothermics.2021.102238.

Jolivet, R. & Frank, W., 2020. The transient and intermittent nature of slow slip, *AGU Adv.,* **1**(1), e2019AV000126. doi:10.1029/2019AV000126.

Jolivet, R., Candela, T., Lasserre, C., Renard, F., Klinger, Y. & Doin, M.-P., 2015. The burst-like behavior of aseismic slip on a rough fault: the creeping section of the Haiyuan fault, China, *Bull. seism. Soc. Am.,* **105**(1), 480–488.

Koirala, R., Kwiatek, G., Shirzaei, M., Brodsky, E., Cladouhos, T., Swyer, M. & Goebel, T., 2024. Induced seismicity and surface deformation associated with long-term and abrupt geothermal operations in blue mountain, Nevada, *Earth planet. Sci. Lett.,* **643,** 118 883. doi:10.1016/j.epsl.2024.118883.

Langenbruch, C., Dinske, C. & Shapiro, S., 2011. Inter event times of fluid induced earthquakes suggest their poisson nature, *Geophys. Res. Lett.,* **38**(21), doi:10.1029/2011GL049474.

Lengliné, O., Boubacar, M. & Schmittbuhl, J., 2017a. Seismicity related to the hydraulic stimulation of GRT1, Rittershoffen, France, *Geophys. J. Int.,* **208**(3), 1704–1715.

Lengliné, O. *et al.*, 2023. The largest induced earthquakes during the GEOVEN deep geothermal project, Strasbourg, 2018–2022: from source parameters to intensity maps, *Geophys. J. Int.,* **234**(3), 2445–2457.

Lengliné, O., Frank, W.B., Marsan, D. & Ampuero, J.-P., 2017b. Imbricated slip rate processes during slow slip transients imaged by low-frequency earthquakes, *Earth planet. Sci. Lett.,* **476,** 122–131.

Majer, E.L., Baria, R., Stark, M., Oates, S., Bommer, J., Smith, B. & Asanuma, H., 2007. Induced seismicity associated with enhanced geothermal systems, *Geothermics,* **36**(3), 185–222.

Martínez-Garzón, P., Kwiatek, G., Sone, H., Bohnhoff, M., Dresen, G. & Hartline, C., 2014. Spatiotemporal changes, faulting regimes, and source parameters of induced seismicity: a case study from the geysers geothermal field, *J. Geophys. Res. Solid Earth,* **119**(11), 8378–8396.

MathWorks, I., 2020. Matlab version: 9.9.0 (r2020b). https://www.mathworks.com (accessed April 2025).

Maurer, V., Cuenot, N., Richard, A., Peterschmitt, A. & Ravier, G., 2020a. Geophysical monitoring of geothermal fields in the upper rhine graben, in *Proceedings World Geothermal Congress,* Reykjavik, Iceland.

Maurer, V., Gaucher, E., Grunberg, M., Koepke, R., Pestourie, R. & Cuenot, N., 2020b. Seismicity induced during the development of the Rittershoffen geothermal field, France, *Geotherm. Energy,* **8**(1), 5. doi:0.1186/s40517-020-0155-2.

Meller, C., Kontny, A. & Kohl, T., 2014. Identification and characterization of hydrothermally altered zones in granite by combining synthetic clay content logs with magnetic mineralogical investigations of drilled rock cuttings, *Geophys. J. Int.,* **199**(1), 465–479.

Neuville, A., Toussaint, R. & Schmittbuhl, J., 2010. Hydrothermal coupling in a self-affine rough fracture, *Phys. Rev. E,* **82**(3), 036 317. doi:10.1103/PhysRevE.82.036317.

Park, Y., Mousavi, S.M., Zhu, W., Ellsworth, W.L. & Beroza, G.C., 2020. Machine-learning-based analysis of the Guy-Greenbrier, Arkansas earthquakes: A tale of two sequences, *Geophys. Res. Lett.,* **47**(6), e2020GL087032. doi:10.1029/2020GL087032.

Pribnow, D. & Schellschmidt, R., 2000. Thermal tracking of upper crustal fluid flow in the Rhine Graben, *Geophys. Res. Lett.,* **27**(13), 1957–1960.

Salaun, N., Toubiana, H., Mitschler, J.-B., Gigou, G., Carriere, X., Maurer, V. & Richard, A., 2020. High-resolution 3-D seismic imaging and refined velocity model building improve the image of a deep geothermal reservoir in the upper Rhine Graben, *Leading Edge,* **39**(12), 857–863.

Sanjuan, B., Millot, R., Innocent, C., Dezayes, C., Scheiber, J. & Brach, M., 2016. Major geochemical characteristics of geothermal brines from the Upper Rhine Graben granitic basement with constraints on temperature and circulation, *Chem. Geol.,* **428,** 27–47.

Schultz, R., Park, Y., Aguilar Suarez, A.L., Ellsworth, W.L. & Beroza, G.C., 2023. En echelon faults reactivated by wastewater disposal near Musreau lake, Alberta, *Geophys. J. Int.,* **235**(1), 417–429.

Shapiro, S.A. & Dinske, C., 2009. Fluid-induced seismicity: pressure diffusion and hydraulic fracturing, *Geophys. Prospect.,* **57**(2), 301–310.

Trugman, D.T. & Shearer, P.M., 2017. Growclust: a hierarchical clustering algorithm for relative earthquake relocation, with application to the spanish springs and Sheldon, Nevada, earthquake sequences, *Seismol. Res. Lett.,* **88**(2A), 379–391.

Vidal, J., Genter, A. & Schmittbuhl, J., 2016. Pre-and post-stimulation characterization of geothermal well GRT-1, Rittershoffen, France: insights from acoustic image logs of hard fractured rock, *Geophys. J. Int.,* **206**(2), 845–860.

Vidal, J., Hehn, R., Glaas, C. & Genter, A., 2019. How can temperature logs help identify permeable fractures and define a conceptual model of fluid circulation? an example from deep geothermal wells in the upper Rhine Graben, *Geofluids,* **2019**(1), 3978 364. doi:10.1155/2019/3978364.

Wessel, P., Luis, J.F., Uieda, L.a. , Scharroo, R., Wobbe, F., Smith, W.H. & Tian, D., 2019. The generic mapping tools version 6, *Geochem. Geophys. Geosyst.,* **20**(11), 5556–5564.

Williams, T. *et al.*, 2010. program Gnuplot 4.4: an interactive plotting. http://gnuplot.sourceforge.net/ (accessed April 2025).

Wintsch, R., Christoffersen, R. & Kronenberg, A., 1995. Fluid-rock reaction weakening of fault zones, *J. Geophys. Res. Solid Earth,* **100**(B7), 13 021–13 032.

Wu, C., Guyer, R., Shelly, D., Trugman, D., Frank, W., Gomberg, J. & Johnson, P., 2015. Spatial-temporal variation of low-frequency earthquake bursts near Parkfield, California, *Geophys. J. Int.,* **202**(2), 914–919.

Wynants-Morel, N., Cappa, F., De Barros, L. & Ampuero, J.-P., 2020. Stress perturbation from aseismic slip drives the seismic front during fluid injection in a permeable fault, *J. Geophys. Res. Solid Earth,* **125**(7), e2019JB019179. doi:10.1029/2019JB019179.

Yasuhara, H. & Elsworth, D., 2006. A numerical model simulating reactive transport and evolution of fracture permeability, *Int. J. Numer. Anal. Methods Geomech.,* **30**(10), 1039–1062.

Yehya, A. & Rice, J.R., 2020. Influence of fluid-assisted healing on fault permeability structure, *J. Geophys. Res. Solid Earth,* **125**(10), e2020JB020553. doi:10.1029/2020JB020553.

Zang, A., Oye, V., Jousset, P., Deichmann, N., Gritto, R., McGarr, A., Majer, E. & Bruhn, D., 2014. Analysis of induced seismicity in geothermal reservoirs–an overview, *Geothermics,* **52,** 6–21.

Zhou, W., Lanza, F., Grigoratos, I., Schultz, R., Cousse, J., Trutnevyte, E., Muntendam-Bos, A. & Wiemer, S., 2024. Managing induced seismicity risks from enhanced geothermal systems: A good practice guideline, *Rev. Geophys.,* **62**(4), e2024RG000849. doi:10.1029/2024RG000849.